Additive Manufacturing Letters 3 (2022) 100045

Contents lists available at ScienceDirect

Additive Manufacturing Letters

journal homepage: www.elsevier.com/locate/addlet

Short Communication

# A Process Parameter Predictive Framework for Laser Cladding of Multi-principal Element Alloys

Praveen Sreeramagiri, Ganesh Balasubramanian*

*Department of Mechanical Engineering & Mechanics, Lehigh University, Bethlehem, PA 18015*

ARTICLE INFO

*Keywords:*
multi-principal element alloys
additive manufacturing
diffusion coefficient
crystallographic phase
cooling rate
Pareto front

ABSTRACT

Surface engineering by additive manufacturing of multi-principal element alloys (MPEAs) has generated significant attention recently for the range of remarkable material properties that can be achieved. A challenge exists in determining the optimum processing parameters for fabricating alloys of various compositions, as they govern the quality of the deposited material. Nevertheless, only limited models are available to predict the initial parameter window for the processing parameters. Using AlCoCrFeNi MPEA as a testbed for laser metal deposition, we present a framework correlating material properties to processing variables coupling predictions from fundamental molecular simulations and meta-heuristic optimization approaches. A set of dimensionless objective functions are constructed to connect elemental diffusion and atomic radii to the macroscopic process parameters, *viz.,* cooling rate, energy density and powder deposition density. Our results suggest that the diffusion coefficient varies exponentially with cooling rate, when the MPEA assumes a crystalline phase upon solidification due to the formation of crystal point defects and a high activation energy rate required for diffusion during rapid cooling. However, the absence of these defects in an amorphous phase of the alloy renders no definitive correlation for the elemental diffusion coefficients with varying cooling rates. Through a multi-objective cuckoo search optimization, we construct a Pareto front to identify optimal values for processing variables, which concur with the parameters adopted in the literature for laser cladding of complex alloys.

## 1. Laser Cladding of MPEAs

Multi-principal element alloys (MPEAs) have gained immense interest over the past decade [1–6] owing to their exceptional phase stabilities and potential for notable mechanical properties at elevated temperatures. Several MPEAs assume a single phase (concentrated and random) solid-solution lattice structure as either fcc [7], bcc [8] or hcp [9]. Being precipitate independent, the lattice distortions and strain hardening in these solid-solutions promote excellent material properties relative to conventional (precipitate strengthened) alloys [10]. These advantages encourage the use of MPEAs for coating applications by surface engineering [11] to significantly improve toughness and wear resistance, and retard the formation and propagation of cracks.

Laser-deposition based surface engineering with MPEAs is a highly viable option for its ease of use and multi-material capabilities at larger scales. Laser metal deposition (LMD), a.k.a. laser cladding or direct laser fabrication (DLF) [11–25] as illustrated in Figure 1, employs a laser as the heat source to melt the feedstock (typically powder or wire) by localized heating to deposit the coating material on the substrate [26]. Albeit the advantages of scalability and compositional gradation in material deposition, certain materials challenges — hot tears/cracks resulting from inhomogeneous temperature distribution from rapid heating/cooling cycles [26–28], poor degree of intermixing at the interface, and the formation of brittle intermetallics [23] — pose serious problems for fabricating MPEA clads.

The cracks in the MPEAs deposited by LMD processes arise due to residual thermal stresses and incompatibility between the substrate and the powder material, and are predominantly governed by the processing parameters employed during the manufacturing [26–29]. Processing parameters/variables in laser additive manufacturing comprise of the input thermal energy from the laser power $L_p$ (W), scan speed of the laser $V$ (mm/min or mm/sec) and powder flow rate $m$ (gm/min). These parameters directly influence the cooling rate employed on the alloy; the thermal energy input (through $L_p$) and removal (through $V$). Together, these effects drive the elemental diffusion, and consequently the segregation and homogeneity in the clad microstructure. Note that the cooling rates typically used in additive manufacturing processes range between $\sim 10^3 - 10^6$ K/sec [26,30]. Thus, it is vital to deter-

* Corresponding author. Packard Laboratory 561, 19 Memorial Drive West, Bethlehem, PA 18015, USA. Phone: +1-610-758-3784.
*E-mail address:* bganesh@lehigh.edu (G. Balasubramanian).

https://doi.org/10.1016/j.addlet.2022.100045
Received 13 February 2022; Received in revised form 14 March 2022; Accepted 2 April 2022

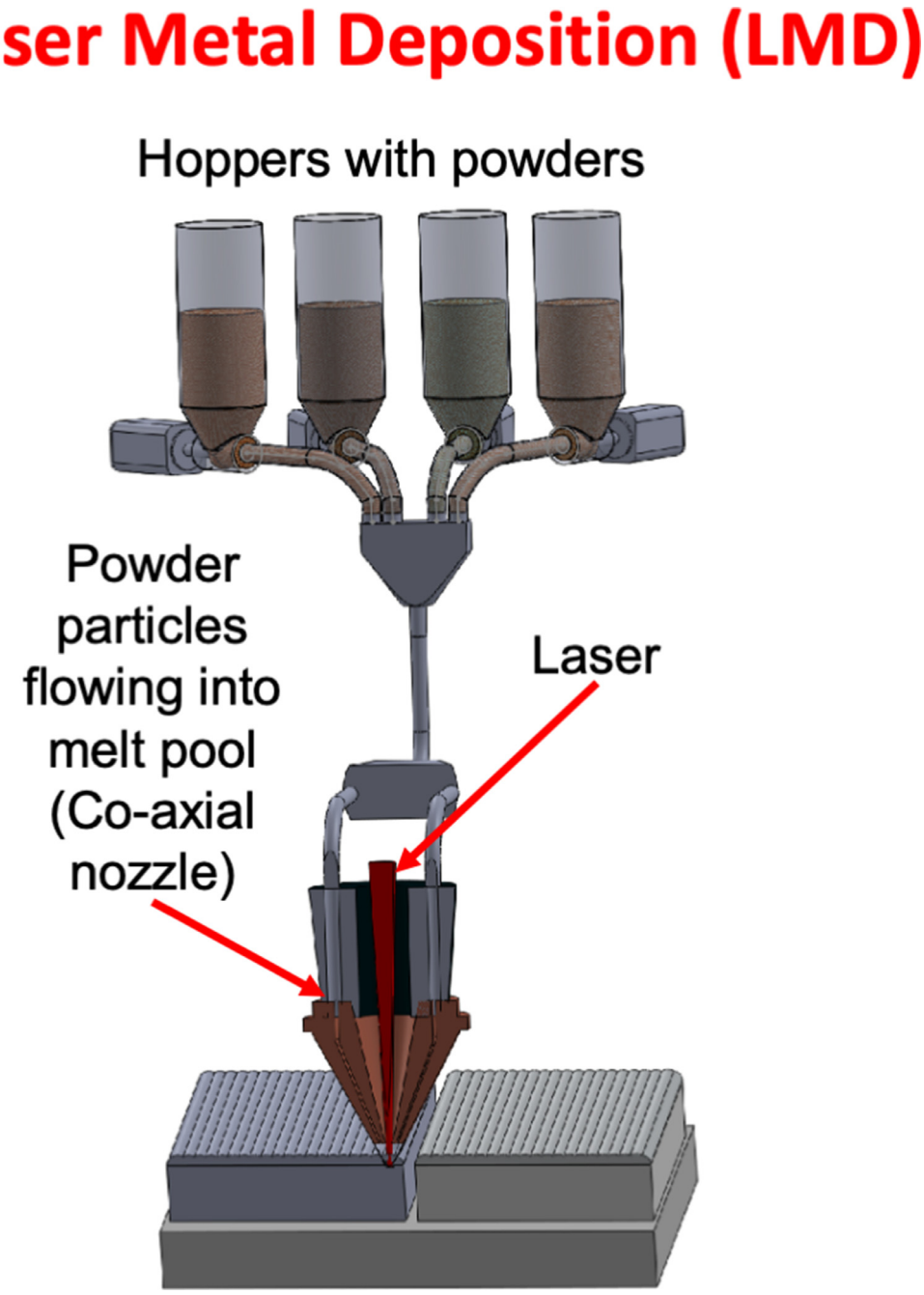


**Figure 1.** Illustration of Laser Metal Deposition: A beam of laser shoots at a point on a surface to create a melt-pool, powder is delivered in the melt pool and as the beam moves away, the molten metal instantly solidifies to form a solid clad, which then continues according to the design to complete the part.

mine the optimal processing parameters for LMD of MPEAs, especially due to the comparable concentrations of multiple metals present in the alloy.

Typically, process parameter optimization initiates with a design of experiments (DoE) in a matrix of the design space with the $L_p$, $V$ and $m$ as the primary variables, as elucidated in Figure 2(a). The optimum design space is then determined iteratively by performing experiments, and visual and microscopic inspections [26,28]. A few computational approaches based on machine learning and physics based multi-modeling techniques [31–33] exist that can optimize the variables after an initial parametric landscape is stipulated. The literature available in this technical domain essentially estimates the processing parameters and residual stresses, predominantly involving thermo-physical properties [34–37] that are relevant for a deeper understanding of the quality of the deposit. Here, in addition to considering MPEA as a testbed that has not been explored extensively in this technical space, we present a framework to correlate the effects of these processing parameters on the material properties that germinate at the atomic scale. Success of this approach will enable a microstructure-controlled additive manufacturing platform for advanced alloys. We propose a framework to directly correlate the macroscopic processing conditions of the laser deposition processes to the nanoscale diffusion of the alloy elements, to aid in our understanding of the melt dynamics, and to predict the initial processing parameter set. We employ this process parameter predictive framework

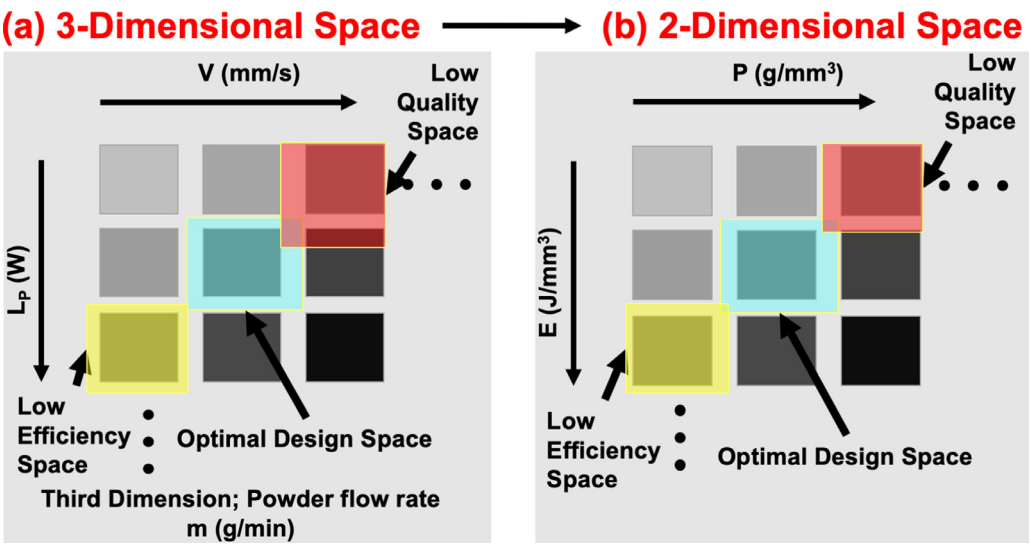


**Figure 2.** **(a)** A 3D landscape for the design of experiments (DoE) comprising the laser power ($L_P$), scan speed ($V$) and the powder flow rate ($m$) being mapped onto **(b)** a 2D domain composed of effective energy per unit volume ($E$) and the powder deposition density ($P$).

for laser cladding of the AlCoCrFeNi MPEA as a testbed, and validate our results with observations in the literature.

## 2. Constructing the predictive framework

### 2.1. Macroscopic Processing Variables

We correlate the macroscopic processing conditions $L_P$, $V$, $m$ and $t_L$ (layer thickness) to the atomistic diffusion of the MPEA melt. First, we perform dimensionality reduction by mapping the 3D space shown in Figure 2(a) onto a 2D domain illustrated in Figure 2(b) using derived processing parameters, *viz.*, energy density $E$ (J/mm$^3$) and powder deposition density $P$ (g/mm$^3$) [18].

$$E = \frac{L_P}{V \times d_b \times t_L}\left(\frac{J}{mm^3}\right) \tag{1}$$

$$P = \frac{m}{V \times d_b \times t_L}\left(\frac{d_b}{d_n}\right)^2\left(\frac{g}{mm^3}\right) \tag{2}$$

Here, $d_b$ is the beam diameter of the laser and $d_n$ the diameter of the nozzle for the powder deposition. These derived physical quantities also facilitate a normalized process modeling for additive manufacturing using a gamut of machines. These parameters implicitly determine the rate at which the alloy is cooled (*i.e.*, cooling rate $C$) from melt to solid, which in turn contributes towards the potential for crack formation. Additionally, we consider the pre-heating temperature of the substrate $T_S$ since it is important in reducing the cooling rate and aids in mitigating crack formation [38].

### 2.2. Material Properties

The material properties of the MPEA, such as the mean atomic radius $R$ and the overall diffusion coefficient $D$, significantly impact the elemental segregation and ultimately the microstructure and properties of the fabricated clad. We consider the molar average to compute the $D$ for the alloy to define a mean metric that can represent the intermixing of all the constituent elements. While physical quantities such as thermal conductivity and specific heat play an important role in determining the quality of manufactured component, the current framework is primarily centered on understanding materials behavior and controlling the processing parameters related to the mixing and fusion of the elemental constituents of the alloy melt as it transitions from the liquid to the solid phase during laser deposition. In that regard, diffusion coefficient of the atoms for the different species present in the melt provides a credible metric to examine the mixing of the candidate elements towards forming solid-solutions. Maximizing the diffusion coefficient permits an enhanced motion of the atoms in the alloy melt, promoting enhanced mixing of the constituent elements and potentially improving the compositional homogeneity. A smaller atomic radius enables faster diffusion. On the contrary, minimizing cooling rate is essential to reduce non-uniform and discontinuous clad tracks, and cracking.

$$R = \sum M_i R_i \tag{3}$$

$$D = \sum M_i D_i \tag{4}$$

$$D_i = \frac{1}{6}\frac{\partial}{\partial x} MSD(\tau) = \frac{1}{6}\frac{\partial}{\partial x}\left(\frac{1}{N}\sum_{j=1}^{N} < (x_j(t) - x_j(0))^2 >\right) \tag{5}$$

Here, $M_i$ is the mole fraction of i$^{th}$ element (0.2 in our case), $R_i$ is the radius of the i$^{th}$ element, $D_i$ is the diffusion coefficient of the i$^{th}$ element, and MSD is the mean squared displacement (Å$^2$) as a function of time $\tau$. These $D$ predictions are empirically correlated with temperature using an Arrhenius model [39] (equation 6), which enables us to obtain the temperature independent diffusion coefficient (diffusion pre-exponential $D_0$) of the MPEA for varying cooling rates (with $T$ = 1600 K, approximately 100 K below the melting temperature $T_m$ of the alloy) [40].

$$D = D_0 \exp\left(-\frac{Q_d}{RT}\right) \tag{6}$$

Given the wide range for the temperature distributions from melt to solidification during additive manufacturing processes, we consider the temperature independent $D_0$ in our framework.

### 2.3. Correlating processing and material parameters

Dimensional analyses of the above defined physical quantities results in two inter-dependent non-dimensional functions, $f_1$ and $f_2$. The underlying mathematics (for the units associated with the physical quantities) involved in constructing these dimensionless quantities is provided as supplementary information.

$$f_1 = \frac{1}{D^*} = \frac{R}{D_0}\sqrt{\frac{E}{P}} \tag{7}$$

$$f_2 = C^* = \frac{CR}{T_S}\sqrt{\frac{P}{E}} \tag{8}$$

$D^*$ and $C^*$ represent dimensionless diffusion coefficient and cooling rate, respectively. Maximizing $D_0$ (i.e., minimizing $1/D^*$), which is the temperature independent characteristic diffusion coefficient for the alloy at a prescribed cooling rate, will permit an enhanced motion of the atoms in the alloy melt, contributing to superior mixing of the molten metal and potentially creating clads with single phase solid-solutions. On the contrary, minimizing $C^*$ is essential to reduce non-uniform and discontinuous clad tracks, and cracking. Note that the correlations are pair-wise intuitive, *e.g.*, a smaller $R$ will enhance $D^*$ while reducing $C^*$, and so on. Thus, a multi-objective optimization problem is set up where a potential tradeoff between $D_0$ and $C$, using a Pareto front for $f_1 - f_2$ mapping, drives the selection of the processing conditions. We use $10 < E < 210$ J/mm$^3$ & $0 < P < 6.9\times10^{-4}$ g/mm$^3$ as the processing boundaries of our problem, based on the commonly adopted conditions for several alloys in the literature [18,32].

### 2.3. Multi-Objective Optimization

We employ a multi-objective cuckoo search (MOCS) [41] technique to minimize our objective functions $f_1$ and $f_2$. MOCS is inspired by the brood parasitism of cuckoo birds that are known for their aggressive reproduction strategy. The general workflow, described in details as supplementary information, involves the following basic concepts: (i) Every cuckoo lays $N$ eggs, which corresponds to $N$ possible solutions and deposits them in random nests at a given time $t$. (ii) A probability function is employed to discard each nest with a probability $p_a \in [0,1]$ and generate a new nest with $N$ eggs accounting for the survivability of the eggs being considered. The nest generation is performed by random walk or Lévy flight approaches and these solutions are evaluated at the same instance. Cuckoo search utilizes the Lévy flight mechanism to determine the step length by a Lévy distribution, $L(s) = \frac{\alpha\beta\Gamma(\beta)\sin(\frac{\pi\beta}{2})}{\pi s^{1+\beta}}$, ($s \gg 0$), with $\Gamma(\lambda)$ being the gamma function. To generate new solutions $x^{(t+1)}$ for nest $i$, a Lévy flight is performed as $x_i^{t+1} = x_i^t + \alpha \otimes \mathrm{L}(s,\beta)$, with $\alpha\ (>0) = \alpha_0(x_j^t - x_i^t)$, where the constant $\alpha_0$ is the step-size scaling factor, and $\otimes$ represents the entry-wise product of the parameters. To discard the nests consisting of the unfavorable solutions, we select a switching parameter/fraction $p_a = 0.25$, reported previously to describe a minimal dependence on the convergence of the optimization approach [42].

## 3. Discussion of the predictions

We employ molecular dynamics (MD) simulations to estimate the diffusion coefficients of elements in the alloy melt as a function of cooling rate. The use of this computational technique circumvents the challenges associated with experimental measurements of these properties, but more importantly offers fundamental insights on the material processes during the manufacturing. The details of the computations are provided as supplementary information. Our choice of interatomic potentials has been validated previously to accurately describe the structural properties of this five-component alloy [43,44]. We examine the MSD of the alloy as a function of time to determine the temperature dependent diffusion coefficients $D$ (at 2200 K, 2000 K, 1900 K, 1600 K) for several cooling rates, with the objective of maximizing the elemental diffusion in the melt to promote enhanced mixing in the alloy during processing. Nevertheless, the length scale employed in the MD simulations restricts our computations from analyzing the diffusion in polycrystalline cases.

### 3.1. Diffusion pre-exponential ($D_0$)

The variation of the MSD with time for the MPEA at various temperatures is presented in Figure 3(a), and the corresponding $D_0$ predictions for a cooling rate of $5\times10^8$ K/s are listed in Table 1. Using the Arrhenius model, we obtain the activation energy $Q_d$ and $D_0$ from Figure 3(b). Likewise, the characteristic diffusion coefficients $D_0$ for representative possible cooling rates ranging from $2.5\times10^8$ K/s to $\sim10^{12}$ K/s are evaluated and reproduced in Figure 3(c). To assert the accuracy of our results, we refer to the validation of the crystallographic phases of this MPEA as a function of the cooling rate reported previously [43,44] with the critical cooling rate being $2.5\times10^{10}$ K/s. In addition, our predictions of the diffusion coefficients strongly concur with prior literature [45,46] and we note a sluggish diffusion, distinctive to MPEAs, reported previously [40,47].

The predictions for $D_0$ emphasize the importance of the crystallographic phases formed during the cooling, as observed from Figure 3(c). The scatter in our predictions for the diffusion coefficients is attributed to the possible sampling errors associated with co-existence of several elements, and potentially multiple phases, even if small fractions, within the MPEA. Such a dispersion in data is more pronounced for the amorphous material that does not assume a preferential crystallographic phase. Nonetheless, an exponential correlation (Equation 9) between $D_0$ and $C$ is empirically established for the MPEA when it solidifies into a crystalline phase. In addition, the minimal change noted in $D_0$ with varying cooling rates corroborates with literature that evinces of sluggish diffusion for MPEAs even at low cooling rates [40,47].

$$D_0 = a\,(C)^b + c \tag{9}$$

where $a = 4.719\times10^{-7}\frac{m^2}{s^{1-b}K^b}$, $b = -0.013$, $c = -2.32\times10^{-7}\frac{m^2}{s}$.

However, when the alloy solidifies into an amorphous phase, under rapid cooling rates > critical cooling rate of $2.5\times10^{10}$ K/s, no trends are identified for the variations in $D_0$. The dependence of diffusion coefficients on cooling rate in crystalline phases is primarily attributed to the formation of point defects [48] and the migration/exchange of atoms through these point defects. As the cooling rate increases, the migration of atoms in the lattice is effectively suppressed with an associated high rate of activation energy required [48]. An increased cooling rate reduces the time for the atoms to re-arrange themselves in the point defects of the lattice during solidification. Therefore, the point defects, coupled with the time constraint during cooling, promote the diffusion coefficients to exhibit a trend similar to that presented in Figure 3(c). On the contrary, in the amorphous phase the atoms can move within the alloy unconstrained to any lattice sites.

MD simulations are limited on the cooling rates that can be implemented in the computations to generate predictions within a reasonable time. Nevertheless, analogous to the linear regression models adopted previously [49], we extrapolate predictions for $D_0$ at lower cooling rates from equation (9). A wide array of plausible results populated at random intervals are presented in Figure 4, which describe a representative set of combinations for functions $f_1$ and $f_2$.

### 3.2. Pareto Optimal Solution

The quality of the MPEA clad (*i.e.,* reduced occurrences of cracks and their propagations) can be improved by minimizing both the inverse of the dimensionless diffusion coefficient $1/D^*$ and the dimensionless cooling rate $C^*$ functions using the MOCS. This interplay of the contrasting material and process parameters effectively leads to a Pareto front as identified in Figure 4. The trade-off factor ($0 < w < 1$) for balancing the objective functions $f_1$ and $f_2$ can be represented as $f = (w)f_1 + (1-w)f_2$. The trade-off factor assists us to ascribe relative importance to the material and processing parameters to obtain the desired optimal solutions.

We interrogate the MOCS algorithm to ascertain optimum predictions for $E$, $P$ and cooling rate. We consider the limiting boundaries for $E$ and $P$, typically used for laser deposition of metals, as highlighted above. Since the minimum cooling rate yields a maximum diffusion coefficient, we obtain an optimal cooling rate of $10^4$ K/s, in agreement with literature on LMD processes [27,50], which offers a preliminary validation of the predictive framework. Next, to identify the optimum process parameters, we narrow the plausible processing conditions based on the trade-off factors adopted for initial generations of nests (between 0.21

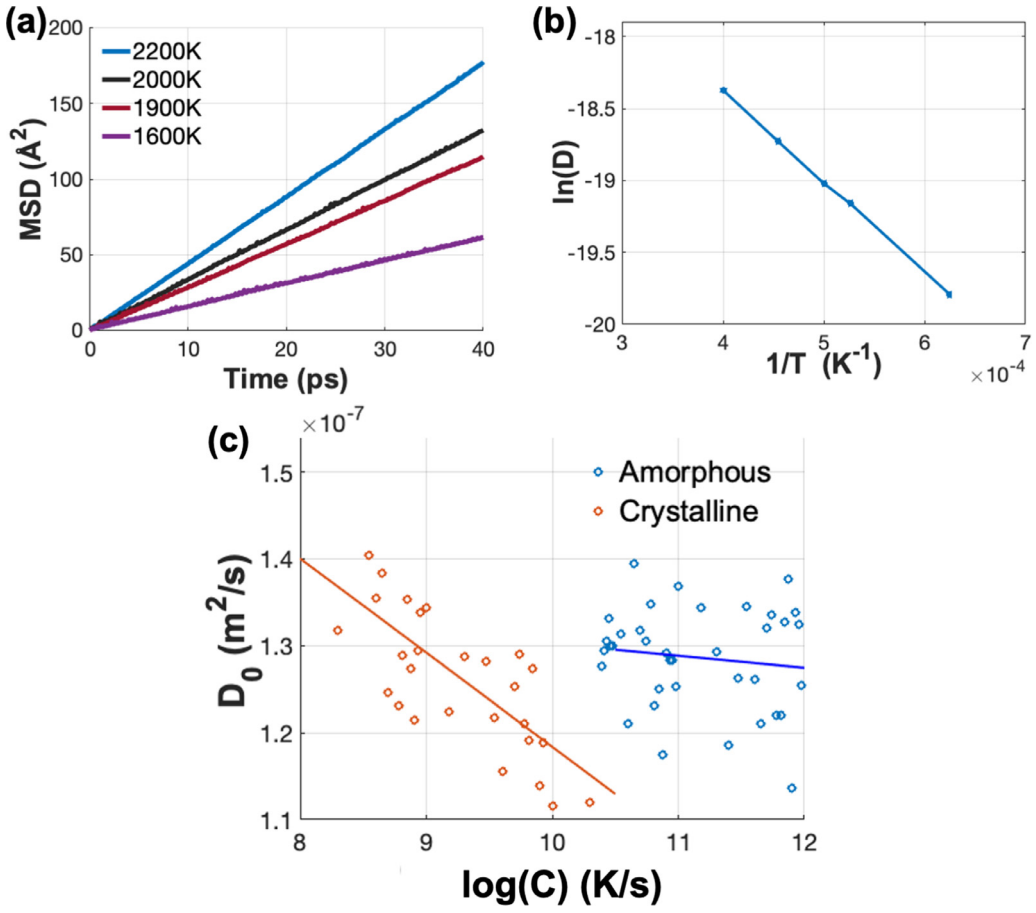


**Figure 3.** (a) Mean squared displacement as a function of simulation time to estimate the diffusion coefficient as a function of the melt temperature. (b) The variation of the natural logarithm of diffusion coefficients $D$ with the inverse of temperature aids in estimating the activation energy and the temperature independent diffusion coefficient (*i.e.,* diffusion pre-exponential $D_0$). (c) The diffusion coefficient $D_0$ (temperature independent) as a function of the cooling rate for crystalline and amorphous phase formations.

**Table 1**
Diffusion coefficients as a function of temperature, the activation energy and the temperature independent diffusion coefficient (diffusion pre-exponential) for the AlCoCrFeNi MPEA melt.

| Cooling Rate $C$ (K/s) | Temperature $T$ (K) | Diffusion coefficient $D$ ($m^2$/s) | Activation energy $Q_d$ (kJ) | Diffusion Pre-Exponential $D_0$ ($m^2$/s) |
|---|---|---|---|---|
| $5 \times 10^8$ | 2200 | $7.36 \times 10^{-9}$ | 51.78 | $1.25 \times 10^{-7}$ |
| | 2000 | $5.49 \times 10^{-9}$ | | |
| | 1900 | $4.77 \times 10^{-9}$ | | |
| | 1600 | $2.54 \times 10^{-9}$ | | |

$< w < 0.55$), and continue the iterations. This procedure ensures both $f_1$ and $f_2$ are minimized. Upon successive iterations implementing the desired trade-offs, any combination of the objective functions that lie on the Pareto front represents an optimal solution. The results from this predictive framework for AlCoCrFeNi MPEA, listed in Table 2, strongly align with those reported in the literature (as compared in Table 2) [51–54] for energy densities ranging between $\sim 40 \leq E \leq 115$ J/mm$^3$. Our framework can be adapted to any material system, provided the diffusion coefficients as a function of cooling rates are estimated *a priori*.

In addition, our model can be tailored for a variety of metal deposition processes by incorporating the specific processing parameters tunable in the machine. These possibilities include the beam diameter ($d_b$), nozzle diameter ($d_N$), the high/low limits of laser power, scan speed, which constitute the fundamental variables for $E$ and $P$. These machine specific parameters can be adopted as an alternate for the variables in the objective functions to search and obtain a range of conditions for

**Table 2**
Powder deposition density (P) and energy density (E) predictions obtained from Cuckoo Search for a range of trade-off ($0.21 < w < 0.55$) between the objective functions $f_1$ & $f_2$.

| w | P (gm/mm$^3$) | E (J/mm$^3$) | E (J/mm$^3$) (Literature) |
|---|---|---|---|
| 0.21 | 0.000439 | 104.89 | |
| 0.24 | 0.000583 | 114.00 | |
| 0.28 | 0.000489 | 79.94 | 76.92 [53] |
| 0.31 | 0.000683 | 94.52 | |
| 0.34 | 0.000463 | 54.80 | 57.69 [52,54] |
| 0.38 | 0.000467 | 47.59 | 47.1 [51] |
| 0.41 | 0.000673 | 59.38 | 57.69 [52,54] |
| 0.45 | 0.000687 | 52.66 | 47.1 [51] |
| 0.48 | 0.000622 | 41.52 | |
| 0.52 | 0.000689 | 40.02 | |
| 0.55 | 0.000690 | 40.00 | |

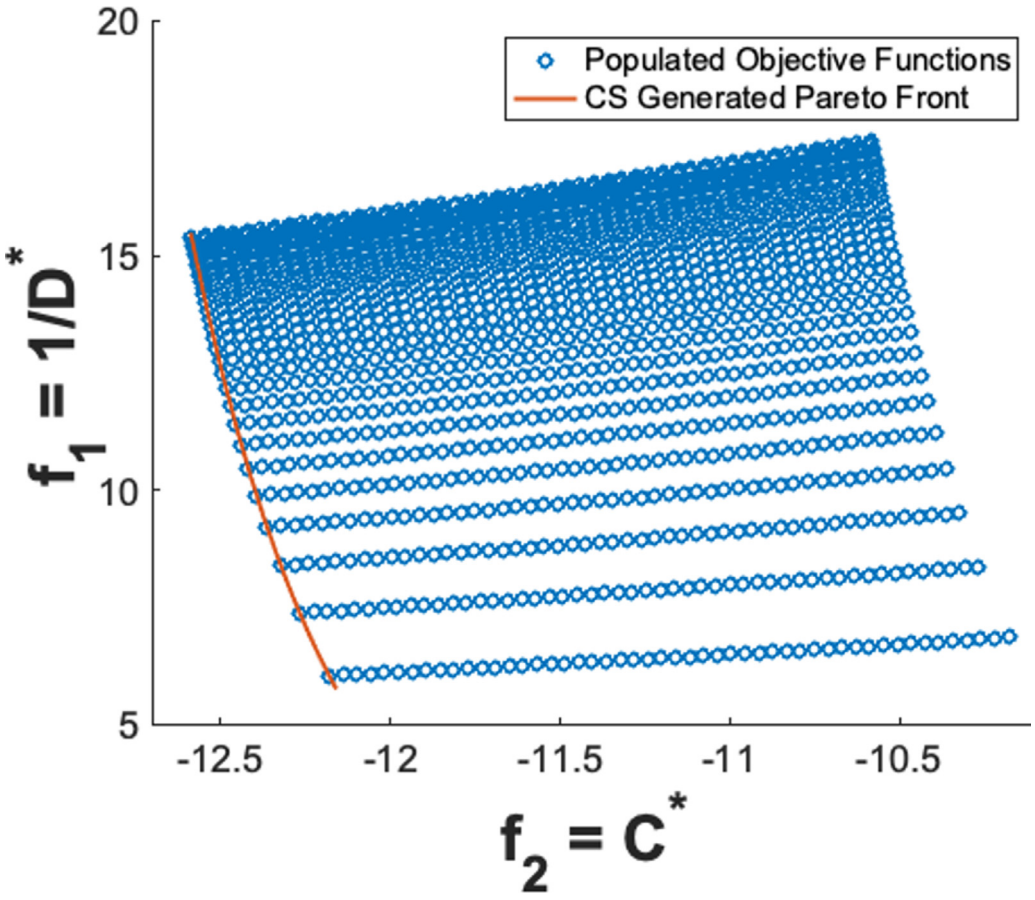


**Figure 4.** Plausible solutions for $f_1$ and $f_2$ based on the exponential correlation of $D_0$ and cooling rate are used to identify the Pareto front, and subsequently the pareto optimal solutions through the multi-objective cuckoo search approach.

the initial DoE to serve as a starting point for any metal additive manufacturing process.

## 4. Summary

We present a framework to predict the processing parameters for the laser additive manufacturing as they govern the quality of the deposited clad. Our model can directly correlate the microscopic material properties like diffusion coefficient, to the macroscopic processing conditions like cooling rate, energy density and powder deposition density. A dimensional analysis enables us to construct two interdependent objective functions that are to be minimized to enhance the quality of the clad and prevent cracking. We employ MD simulations to evaluate the diffusion coefficients of the MPEA for a range of cooling rates between $2.5 \times 10^8$ K/s to $\sim 10^{12}$ K/s. We find the diffusion coefficient to vary exponentially with cooling rate when the alloy solidifies into a crystalline phase (for cooling rates $< 2.5 \times 10^{10}$ K/s). This dependency is attributed to the migration/exchange of atoms between the point defects that occurs during solidification. On the contrary, the diffusion coefficient for an amorphous structure is independent of the cooling rate ($\geq 2.5 \times 10^{10}$ K/s). We use this exponential correlation with a multi-objective cuckoo search algorithm to identify optimal processing conditions through a Pareto front. Minimizing the objective functions promotes an enhanced motion of the atoms in the liquid melt by maximizing the diffusion and retarded cooling rates. All plausible processing conditions that adhere to Pareto optimal solutions can produce a high quality clad. We validate our model with AlCoCrFeNi MPEA as a testbed, with our results *viz.,* $40 \leq E \leq 115$ J/mm$^3$, in excellent agreement with reports in the literature. Besides AlCoCrFeNi MPEA, our framework can estimate the process parameters for any material system, provided the diffusion coefficients as a function of cooling rate are estimated *a priori.*

## Data Availability

The data reported in this paper is available from the corresponding author upon reasonable request.

## Declaration of Competing Interest

The authors declare that they have no known competing financial interests or personal relationships that could have appeared to influence the work reported in this paper.

## Acknowledgements

The research was supported by the National Science Foundation (NSF) through the awards # CMMI-1944040 and OAC-2019035. Any opinions, findings, conclusions or recommendations expressed in this material are those of the authors' and do not necessarily reflect the views of the NSF. The authors thank Drs. Joydeep Munshi, Ankit Roy and Anton van Beek for useful discussions on the computational techniques.

## Supplementary materials

Supplementary material associated with this article can be found, in the online version, at doi:10.1016/j.addlet.2022.100045.

## References


[1] M.C. Gao, P.K. Liaw, D.B. Miracle, FUNDAMENTAL UNDERSTANDING AND APPLICATIONS OF HIGH-ENTROPY ALLOYS, Journal of Materials Research 33 (2018) 2853–2854, doi:10.1557/jmr.2018.347.

[2] S. Gorsse, D.B. Miracle, O.N. Senkov, Mapping the world of complex concentrated alloys, Acta Materialia 135 (2017) 177–187, doi:10.1016/j.actamat.2017.06.027.

[3] S. Gorsse, J.P. Couzinié, D.B. Miracle, From high-entropy alloys to complex concentrated alloys, Comptes Rendus Physique 19 (2018) 721–736, doi:10.1016/j.crhy.2018.09.004.

[4] D.B. Miracle, O.N. Senkov, A critical review of high entropy alloys and related concepts, Acta Materialia 122 (2017) 448–511, doi:10.1016/j.actamat.2016.08.081.

[5] D.B. Miracle, High entropy alloys as a bold step forward in alloy development, Nature Communications 10 (2019) 1–3, doi:10.1038/s41467-019-09700-1.

[6] B. Gludovatz, A. Hohenwarter, D. Catoor, E.H. Chang, E.P. George, R.O. Ritchie, A fracture-resistant high-entropy alloy for cryogenic applications, Science 345 (2014) 1153–1158, doi:10.1126/science.1254581.

[7] Z. Wu, H. Bei, F. Otto, G.M. Pharr, E.P. George, Recovery, recrystallization, grain growth and phase stability of a family of FCC-structured multi-component equiatomic solid solution alloys, Intermetallics 46 (2014) 131–140, doi:10.1016/j.intermet.2013.10.024.

[8] O.N. Senkov, J.M. Scott, S.V. Senkova, D.B. Miracle, C.F. Woodward, Microstructure and room temperature properties of a high-entropy TaNbHfZrTi alloy, Journal of Alloys and Compounds 509 (2011) 6043–6048, doi:10.1016/j.jallcom.2011.02.171.

[9] Y.J. Zhao, J.W. Qiao, S.G. Ma, M.C. Gao, H.J. Yang, M.W. Chen, Y. Zhang, A hexagonal close-packed high-entropy alloy: The effect of entropy, Materials and Design 96 (2016) 10–15, doi:10.1016/j.matdes.2016.01.149.

[10] A. Roy, P. Sreeramagiri, T. Babuska, B. Krick, P.K. Ray, G. Balasubramanian, Lattice distortion as an estimator of solid solution strengthening in high-entropy alloys, Materials Characterization 172 (2021) 110877, doi:10.1016/j.matchar.2021.110877.

[11] Y.P. Kathuria, Some aspects of laser surface cladding in the turbine industry, Surface and Coatings Technology 132 (2000) 262–269, doi:10.1016/S0257-8972(00)00735-0.

[12] Z. Wang, A. Genc, I. Baker, Direct versus indirect particle strengthening in a strong, ductile FeNiMnAlTi high entropy alloy, Materials Characterization 132 (2017) 156–161, doi:10.1016/j.matchar.2017.08.019.

[13] C. Lee, X. Wei, J.W. Kysar, J. Hone, Measurement of the Elastic Properties and Intrinsic Strength of Monolayer Graphene, Science 321 (2008) 385–388, doi:10.1126/science.1157996.

[14] K.V.S. Thurston, B. Gludovatz, A. Hohenwarter, G. Laplanche, E.P. George, R.O. Ritchie, Effect of temperature on the fatigue-crack growth behavior of the high-entropy alloy CrMnFeCoNi, (2017). https://doi.org/10.1016/j.intermet.2017.05.009.

[15] K.V.S. Thurston, B. Gludovatz, Q. Yu, G. Laplanche, E.P. George, R.O. Ritchie, Temperature and load-ratio dependent fatigue-crack growth in the CrMnFeCoNi high-entropy alloy, Journal of Alloys and Compounds 794 (2019) 525–533, doi:10.1016/j.jallcom.2019.04.234.

[16] Y. Brif, M. Thomas, I. Todd, The use of high-entropy alloys in additive manufacturing, Scripta Materialia 99 (2015) 93–96, doi:10.1016/j.scriptamat.2014.11.037.

[17] S.Y. Chen, Y. Tong, P.K. Liaw, Additive manufacturing of high-entropy alloys: A Review, Entropy 20 (2018) 12, doi:10.3390/e20120937.

[18] S. Gorsse, C. Hutchinson, M. Gouné, R. Banerjee, Additive manufacturing of metals: a brief review of the characteristic microstructures and properties of steels, Ti-6Al-4V and high-entropy alloys, Science and Technology of Advanced Materials 18 (2017) 584–610, doi:10.1080/14686996.2017.1361305.

[19] B. Gwalani, V. Soni, O.A. Waseem, S.A. Mantri, R. Banerjee, Laser additive manufacturing of compositionally graded AlCrFeMoVx (x = 0 to 1) high-entropy alloy system, Optics and Laser Technology 113 (2019) 330–337, doi:10.1016/j.optlastec.2019.01.009.

[20] O.N. Senkov, G.B. Wilks, J.M. Scott, D.B. Miracle, Mechanical properties of Nb25Mo25Ta 25W25 and V20Nb20Mo 20Ta20W20 refractory high entropy alloys, Intermetallics 19 (2011) 698–706, doi:10.1016/j.intermet.2011.01.004.

[21] H. Dobbelstein, E.L. Gurevich, E.P. George, A. Ostendorf, G. Laplanche, Laser metal deposition of compositionally graded TiZrNbTa refractory high-entropy alloys using elemental powder blends, Additive Manufacturing 25 (2019) 252–262, doi:10.1016/j.addma.2018.10.042.

[22] H. Dobbelstein, E.L. Gurevich, E.P. George, A. Ostendorf, G. Laplanche, Laser metal deposition of a refractory TiZrNbHfTa high-entropy alloy, Additive Manufacturing 24 (2018) 386–390, doi:10.1016/j.addma.2018.10.008.

[23] B.A. Welk, R.E.A. Williams, G.B. Viswanathan, M.A. Gibson, P.K. Liaw, H.L. Fraser, Nature of the interfaces between the constituent phases in the high entropy alloy CoCrCuFeNiAl, Ultramicroscopy 134 (2013) 193–199, doi:10.1016/j.ultramic.2013.06.006.

[24] C. Cui, Z. Guo, Y. Liu, Q. Xie, Z. Wang, J. Hu, Y. Yao, Characteristics of cobalt-based alloy coating on tool steel prepared by powder feeding laser cladding, Optics and Laser Technology 39 (2007) 1544–1550, doi:10.1016/j.optlastec.2006.12.005.

[25] A. Emamian, S.F. Corbin, A. Khajepour, Effect of laser cladding process parameters on clad quality and in-situ formed microstructure of Fe-TiC composite coatings, Surface and Coatings Technology 205 (2010) 2007–2015, doi:10.1016/j.surfcoat.2010.08.087.

[26] P. Sreeramagiri, A. Bhagavatam, A. Ramakrishnan, H. Alrehaili, G.P. Dinda, Design and development of a high-performance Ni-based superalloy WSU 150 for additive manufacturing, Journal of Materials Science and Technology 47 (2020) 20–28, doi:10.1016/j.jmst.2020.01.041.

[27] P. Sreeramagiri, A. Bhagavatam, H. Alrehaili, G. Dinda, Direct laser metal deposition of René 108 single crystal superalloy, Journal of Alloys and Compounds 838 (2020) 155634, doi:10.1016/j.jallcom.2020.155634.

[28] A. Ramakrishnan, G.P. Dinda, Direct laser metal deposition of Inconel 738, Materials Science and Engineering: A 740–741 (2019) 1–13, doi:10.1016/j.msea.2018.10.020.

[29] A. Piglione, B. Dovgyy, C. Liu, C.M. Gourlay, P.A. Hooper, M.S. Pham, Printability and microstructure of the CoCrFeMnNi high-entropy alloy fabricated by laser powder bed fusion, Materials Letters 224 (2018), doi:10.1016/j.matlet.2018.04.052.

[30] M.M. Attallah, R. Jennings, X. Wang, L.N. Carter, Additive manufacturing of Ni-based superalloys: The outstanding issues, MRS Bulletin 41 (2016) 758–764, doi:10.1557/mrs.2016.211.

[31] A. Bandyopadhyay, K.D. Traxel, Invited review article: Metal-additive manufacturing—Modeling strategies for application-optimized designs, Additive Manufacturing 22 (2018) 758–774, doi:10.1016/j.addma.2018.06.024.

[32] U. de Oliveira, V. Ocelík, J.T.M. De Hosson, Analysis of coaxial laser cladding processing conditions, Surface and Coatings Technology 197 (2005) 127–136, doi:10.1016/j.surfcoat.2004.06.029.

[33] J.G. Michopoulos, A.P. Iliopoulos, J.C. Steuben, A.J. Birnbaum, S.G. Lambrakos, On the multiphysics modeling challenges for metal additive manufacturing processes, Additive Manufacturing 22 (2018) 784–799, doi:10.1016/j.addma.2018.06.019.

[34] T. Mukherjee, V. Manvatkar, A. De, T. DebRoy, Mitigation of thermal distortion during additive manufacturing, Scripta Materialia 127 (2017) 79–83, doi:10.1016/J.SCRIPTAMAT.2016.09.001.

[35] M. van Elsen, F. Al-Bender, J. Kruth, Application of dimensional analysis to selective laser melting, Rapid Prototyping Journal 14 (2008) 15–22, doi:10.1108/13552540810841526.

[36] B. Rankouhi, A.K. Agrawal, F.E. Pfefferkorn, D.J. Thoma, A dimensionless number for predicting universal processing parameter boundaries in metal powder bed additive manufacturing, Manufacturing Letters 27 (2021) 13–17, doi:10.1016/J.MFGLET.2020.12.002.

[37] T. Mukherjee, V. Manvatkar, A. De, T. DebRoy, Dimensionless numbers in additive manufacturing, Journal of Applied Physics 121 (2017) 064904, doi:10.1063/1.4976006.

[38] E. Toyserkani, A. Khajepour, S.F. Corbin, Laser Cladding, CRC Press, 2004.

[39] J. Ding, M. Asta, R.O. Ritchie, Melts of CrCoNi-based high-entropy alloys: Atomic diffusion and electronic/atomic structure from ab initio simulation, Applied Physics Letters 113 (2018) 111902, doi:10.1063/1.5045216.

[40] A. Roy, J. Munshi, G. Balasubramanian, Low energy atomic traps sluggardize the diffusion in compositionally complex refractory alloys, Intermetallics 131 (2021) 107106, doi:10.1016/j.intermet.2021.107106.

[41] J. Munshi, W. Chen, T.Y. Chien, G. Balasubramanian, Machine learned metaheuristic optimization of the bulk heterojunction morphology in P3HT:PCBM thin films, Computational Materials Science 187 (2021) 110119, doi:10.1016/j.commatsci.2020.110119.

[42] A. Sharma, R. Singh, P.K. Liaw, G. Balasubramanian, Cuckoo searching optimal composition of multicomponent alloys by molecular simulations, Scripta Materialia 130 (2017) 292–296, doi:10.1016/j.scriptamat.2016.12.022.

[43] A. Sharma, S.A. Deshmukh, P.K. Liaw, G. Balasubramanian, Crystallization kinetics in AlxCrCoFeNi ($0 \leq x \leq 40$) high-entropy alloys, Scripta Materialia 141 (2017) 54–57, doi:10.1016/j.scriptamat.2017.07.024.

[44] P. Sreeramagiri, A. Roy, G. Balasubramanian, Effect of cooling rate on the phase formation of AlCoCrFeNi high- entropy alloy, Journal of Phase Equilibria and Diffusion (2021) 1–9, doi:10.1007/S11669-021-00918-5.

[45] C.A. Becker, M.J. Kramer, Atomistic comparison of volume-dependent melt properties from four models of aluminum, Modelling and Simulation in Materials Science and Engineering 18 (2010) 74001, doi:10.1088/0965-0393/18/7/074001.

[46] J. Yuan-Yuan, Z. Quing-Ming, G. Zi-Zheng, J. Guang-Fu, Molecular dynamics simulation of self-diffusion coefficients for liquid metals, Chinese Physics B 22 (2013), doi:10.1088/1674-1056/22/8/083101/meta.

[47] K.-Y. Tsai, M.-H. Tsai, J.-W. Yeh, Sluggish diffusion in Co–Cr–Fe–Mn–Ni high-entropy alloys, Acta Materialia 61 (2013) 4887–4897, doi:10.1016/j.actamat.2013.04.058.

[48] D. Lazarus, DIFFUSION IN CRYSTALLINE AND AMORPHOUS SOLIDS., in: Materials Research Society Symposia Proceedings, Materials Research Soc (1987) 297–311, doi:10.1557/proc-57-297.

[49] A. Roy, T. Babuska, B. Krick, G. Balasubramanian, Machine learned feature identification for predicting phase and Young's modulus of low-, medium- and high-entropy alloys, Scripta Materialia 185 (2020) 152–158, doi:10.1016/j.scriptamat.2020.04.016.

[50] P. Sreeramagiri, G. Balasubramanian, Directed Energy Deposition of Multi-Principal Element Alloys, Frontiers in Materials. In Press (2022).

[51] D. Karlsson, A. Marshal, F. Johansson, M. Schuisky, M. Sahlberg, J.M. Schneider, U. Jansson, Elemental segregation in an AlCoCrFeNi high-entropy alloy – A comparison between selective laser melting and induction melting, Journal of Alloys and Compounds 784 (2019) 195–203, doi:10.1016/j.jallcom.2018.12.267.

[52] R. Wang, K. Zhang, C. Davies, X. Wu, Evolution of microstructure, mechanical and corrosion properties of AlCoCrFeNi high-entropy alloy prepared by direct laser fabrication, 694 (2017) 971–981. https://doi.org/10.1016/j.jallcom.2016.10.138.

[53] V. Ocelík, N. Janssen, S.N. Smith, J.Th.M.de Hosson, Additive Manufacturing of High-Entropy Alloys by Laser Processing, JOM 68 (2016) 1810–1818, doi:10.1007/s11837-016-1888-z.

[54] G. Qin, W. Xue, C. Fan, R. Chen, L. Wang, Y. Su, H. Ding, J. Guo, Effect of Co content on phase formation and mechanical properties of (AlCoCrFeNi)100-Co high-entropy alloys, Materials Science and Engineering: A 710 (2018) 200–205, doi:10.1016/j.msea.2017.10.088.